LEPTONIC AND HADRONIC MODELING OF *FERMI*-DETECTED BLAZARS

M. BÖTTCHER[1,2], A. REIMER[3], K. SWEENEY[2], AND A. PRAKASH[2]

[1] Centre for Space Research, North-West University, Potchefstroom 2531, South Africa
[2] Astrophysical Institute, Department of Physics and Astronomy, Ohio University, Athens, OH 45701, USA
[3] Institut für Theoretische Physik, Universität Innsbruck, Technikerstraße 25, A-6020 Innsbruck, Austria

ABSTRACT

We describe new implementations of leptonic and hadronic models for the broadband emission from relativistic jets in active galactic nuclei in a temporary steady state. For the leptonic model, a temporary equilibrium between particle injection/acceleration, radiative cooling, and escape from a spherical emission region is evaluated, and the self-consistent radiative output is calculated. For the hadronic model, a temporary equilibrium between particle injection/acceleration, radiative and adiabatic cooling, and escape is evaluated for both primary electrons and protons. A new, semianalytical method to evaluate the radiative output from cascades initiated by internal $\gamma\gamma$ pair production is presented. We use our codes to fit snapshot spectral energy distributions (SEDs) of a representative set of *Fermi*-LAT-detected blazars. We find that the leptonic model provides acceptable fits to the SEDs of almost all blazars with parameters close to equipartition between the magnetic field and the relativistic electron population. However, the hard γ-ray spectrum of AO 0235+164, in contrast to the very steep IR–optical–UV continuum, poses a severe problem for the leptonic model. If charge neutrality in leptonic models is provided by cold protons, the kinetic energy carried by the jet should be dominated by protons. We find satisfactory representations of the snapshot SEDs of most blazars in our sample with the hadronic model presented here. However, in the case of two quasars the characteristic break at a few GeV energies cannot be well modeled. All of our hadronic model fits require powers in relativistic protons in the range $L_p \sim 10^{47}$–10^{49} erg s^{-1}.

Key words: galaxies: active – galaxies: jets – gamma rays: galaxies – radiation mechanisms: non-thermal – relativistic processes

Online-only material: color figures

1. INTRODUCTION

Blazars are a class of radio-loud active galactic nuclei (AGNs) comprised of flat-spectrum radio quasars (FSRQs) and BL Lac objects. Their spectral energy distributions (SEDs) are characterized by non-thermal continuum spectra with a broad low-frequency component in the radio–UV or X-ray frequency range and a high-frequency component from X-rays to γ-rays, and they often exhibit substantial variability across the electromagnetic spectrum, in extreme cases on timescales down to just a few minutes. Blazars are subdivided based on the location of their synchrotron peak: low-synchrotron-peaked (LSP) blazars, consisting of FSRQs and low-frequency-peaked BL Lac objects (LBLs) have $\nu_{sy} < 10^{14}$ Hz; intermediate-synchrotron-peaked (ISP) blazars (which are exclusively BL Lac objects and hence also called IBLs or intermediate BL Lac objects) have 10^{14} Hz $\leqslant \nu_{sy} \leqslant 10^{15}$ Hz; high-synchrotron-peaked (HSP) blazars (also exclusively BL Lac objects, called HBLs or high-peaked BL Lac objects) have $\nu_s > 10^{15}$ Hz.

Extreme inferred isotropic luminosities, combined with rapid high-energy variability, provide convincing evidence that the high-energy emission from blazars originates in relativistic jets closely aligned with our line of sight (for a review of those arguments, see, e.g., Schlickeiser 1996). The simplest (and often sufficient) assumption is that the emission is produced in an approximately spherical region, propagating along the jet with a speed $\beta_\Gamma c$, corresponding to a bulk Lorentz factor Γ. If the jet forms an angle θ_{obs} with respect to our line of sight, this results in Doppler boosting characterized by the Doppler factor $D = (\Gamma [1 - \beta_\Gamma \cos \theta_{obs}])^{-1}$. The observed bolometric flux will be enhanced by a factor of D^4, while photon energies are blueshifted by a factor of D, and variability timescales will be shortened by a factor of D^{-1} (for a review of relativistic effects in the jets of AGNs, see Böttcher 2012).

It is generally accepted that the low-frequency (radio through UV or X-ray) emission from blazars is synchrotron emission from relativistic electrons in the jet. For the origin of the high-energy (X-ray through γ-ray) emission, two fundamentally different approaches have been proposed, generally referred to as leptonic and hadronic models.

In leptonic models, the radiative output throughout the electromagnetic spectrum is assumed to be dominated by leptons (electrons and possibly positrons), while any protons that are likely present in the outflow are not accelerated to sufficiently high energies to contribute significantly to the radiative output. The high-energy emission is then most plausibly explained by Compton scattering of low-energy photons by the same electrons producing the synchrotron emission at lower frequencies (Maraschi et al. 1992; Bloom & Marscher 1996; Dermer & Schlickeiser 1993; Sikora et al. 1994; Błażejowski et al. 2000). In hadronic models, both primary electrons and protons are accelerated to ultrarelativistic energies with protons exceeding the threshold for pγ photo-pion production on the soft photon field in the emission region. While the low-frequency emission is still dominated by synchrotron emission from primary electrons, the high-energy emission is dominated by proton-synchrotron emission, π^o decay photons, synchrotron, and Compton emission from secondary decay products of charged pions, and the output from pair cascades initiated by these high-energy emissions intrinsically absorbed by $\gamma\gamma$ pair production (Mannheim

& Biermann 1992; Aharonian 2000; Mücke & Protheroe 2001; Mücke et al. 2003). For a general overview of the features of both leptonic and hadronic blazar models, see Böttcher (2010).

Steady-state leptonic models have met with great success in modeling the SEDs of all classes of blazars (e.g., Ghisellini et al. 1998; Celotti & Ghisellini 2008), including substantial samples of *Fermi*-detected blazars (e.g., Ghisellini et al. 2010). Much progress has also been made to explore the variability features predicted in time-dependent implementations of leptonic models (e.g., Mastichiadis & Kirk 1997; Kusunose et al. 2000; Li & Kusunose 2000; Böttcher & Chiang 2002; Sokolov et al. 2004; Graff et al. 2008; Böttcher & Dermer 2010; Joshi & Böttcher 2011). However, the very fast (timescales of a few minutes) variability of some TeV blazars (Albert et al. 2007; Aharonian et al. 2007) poses severe problems for single-zone models of blazars due to the required extremely high bulk Lorentz factors (Begelman et al. 2008). Even without considering variability, the SED of the quasar 3C 279, detected in very high energy (VHE) γ-rays by MAGIC (Albert et al. 2008), poses problems for one-zone leptonic models, and is more easily represented by a hadronic model (Böttcher et al. 2009). In order to remedy some of the problems, several variations of multi-zone models have been proposed, including the spine-sheath model of Tavecchio & Ghisellini (2008) or the decelerating jet model of Georganopoulos & Kazanas (2003), as well as internal shock models (e.g., Marscher & Gear 1985; Spada et al. 2001; Sokolov et al. 2004; Graff et al. 2008; Joshi & Böttcher 2011; Böttcher & Dermer 2010).

The goal of this work is to provide tools for the modeling of blazar spectra including data from *Fermi*-LAT, which have been accumulated over one year of *Fermi* operations. Any short-term variability in the SEDs of the blazars under consideration, has therefore been averaged out over this integration time. Therefore, for the purpose of this study, we will use time-independent models, which represent an appropriate time average of the rapidly variable broadband emission.

The accurate evaluation of the radiative output of hadronic models is best achieved by Monte Carlo simulations (e.g., Mücke et al. 2000a) due to the complicated energy dependence of the cross sections (in particular, for pγ interactions) involved. As these are quite time-consuming, hadronic models have so far received much less attention in the literature than leptonic ones, and in particular, time-dependent implementations of hadronic models are still in their early development stages. A comparison between the results of fitting a large, statistically representative sample of blazars with both leptonic and hadronic models, considered to comparable degree of detail, has therefore never been performed. This is the main purpose of the code developments and modeling efforts presented in this paper.

In Section 2, we describe recent developments to our existing leptonic radiation transfer code, in particular its application to quasi-stationary situations, and the implementation of arbitrary external radiation fields as sources for Compton scattering. In Section 3, we will describe a new, semianalytical implementation of the stationary hadronic model and test it against results of detailed Monte Carlo simulations based on the SOPHIA code (Mücke et al. 2000a). We present the results of our comparative leptonic and hadronic modeling of the SEDs of a representative sample of *Fermi*-LAT-detected blazars of different subclasses in Section 4. We summarize and discuss our results in Section 5. Throughout our paper, we convert redshifts to luminosity distances using a ΛCDM cosmology with $H_0 = 70$ km s^{-1} Mpc^{-1}, $\Omega_m = 0.3$, and $\Omega_\Lambda = 0.7$.

2. STATIONARY LEPTONIC BLAZAR MODEL

The leptonic jet radiation transfer model used for this work is based on the work of Böttcher & Chiang (2002; see also Böttcher et al. 1997; Böttcher & Bloom 2000). It is a homogeneous one-zone model in which a population of ultrarelativistic electrons (or positrons) is injected with a power-law distribution $Q_e(\gamma_e) = Q_0 \gamma_e^{-q_e} H(\gamma_e; \gamma_{e,1}, \gamma_{e,2})$ into a spherical emission region of comoving radius R. Here, $H(x; a, b)$ is the Heaviside function defined as $H = 1$ if $a \leqslant x \leqslant b$ and $H = 0$ otherwise. The emission region moves with constant relativistic speed $\beta_\Gamma c$ (corresponding to the bulk Lorentz factor Γ) along the jet.

The electron distribution cools due to synchrotron and Compton emission. Synchrotron emission is determined through a tangled magnetic field of comoving strength B. For Compton scattering, the synchrotron radiation field (SSC = synchrotron self-Compton) and various external radiation fields are taken into account: (1) direct accretion disk emission (see Böttcher et al. 1997 for details), (2) accretion disk emission re-processed by the broad-line region (BLR; see Böttcher & Bloom 2000, for details), and (3) an isotropic (in the rest frame of the AGN) external radiation field of arbitrary spectral shape. For the latter, we have developed a pre-processing routine that produces a spectrum file of the external radiation field in the AGN rest frame. The blazar code applies the proper relativistic Lorentz transformations to the blob rest frame to use this radiation field as sources for external Compton scattering. Such a description is appropriate for radiation fields for which the angular characteristics of the radiation field in the comoving frame are dominated by relativistic aberration rather than any intrinsic anisotropy. Quantitatively, the characteristic scale of angular variations $\Delta\theta_{ext}$ of the external radiation field should be $\Delta\theta_{ext} \gg 1/\Gamma$. This is typically the case for (1) (line-dominated) emission from the BLR as long as the emission region is located within the BLR, (2) infrared emission from a large-scale dusty torus around the central engine, and (3) the cosmic microwave background. The external Compton emissivity is evaluated using the head-on approximation for the Compton cross section (based on an angle integration of the full Klein–Nishina cross section; see, e.g., Dermer & Menon 2009). The electron cooling rates due to Compton scattering are calculated using the full Klein–Nishina cross section, adopting the analytical solution of Böttcher et al. (1997). Particles may escape the emission region on a timescale $t_{esc} \equiv \eta_{esc} R/c$, which we parameterize with an escape timescale parameter $\eta_{esc} \geqslant 1$.

In order to fit SEDs of blazars in the absence of detailed spectral variability information, it is appropriate (and computationally more efficient than detailed time-dependent radiation transfer simulations) to apply a stationary radiation transfer model. For the stationary model used in this work, our code finds an equilibrium between the relativistic particle injection mentioned above, radiative cooling, and escape. For this purpose, a critical Lorentz factor γ_c is determined, for which the radiative cooling timescale equals the escape timescale, $\gamma_c/|\dot{\gamma}(\gamma_c)| = t_{esc}$. The shape of the resulting equilibrium particle distribution will then depend on whether $\gamma_c < \gamma_{e,1}$ (the fast cooling regime) or $\gamma_c > \gamma_{e,1}$ (the slow cooling regime). In the fast cooling regime,

$$n_e^{f.c.}(\gamma_e) = n_0 \begin{cases} \left(\frac{\gamma_e}{\gamma_{e,1}}\right)^{-2} & \text{for } \gamma_c \leqslant \gamma_e \leqslant \gamma_{e,1} \\ \left(\frac{\gamma_e}{\gamma_{e,1}}\right)^{-(q_e+1)} & \text{for } \gamma_{e,1} < \gamma_e < \gamma_{e,2} \\ 0 & \text{else} \end{cases} \quad (1)$$
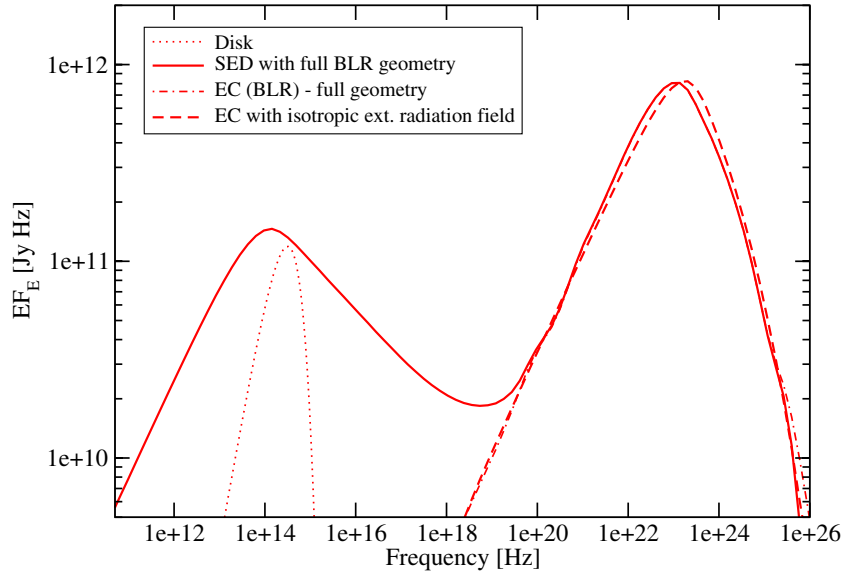
Figure 1. Generic blazar SEDs with EC (BLR) calculated with the full BLR geometry (solid SED; EC (BLR) component: dot-dashed line). The dotted line shows the disk spectrum. The dashed line shows the EC component calculated using an isotropic, thermal external radiation field with a temperature producing the same peak frequency as the disk and the same radiation energy density as resulting from BLR reprocessing of the disk emission.

(A color version of this figure is available in the online journal.)

while in the slow cooling regime,

$$
n_e^{\text{s.c.}}(\gamma_e) = n_0
\begin{cases}
\left(\dfrac{\gamma_e}{\gamma_c}\right)^{-q_e} & \text{for } \gamma_{e,1} \leqslant \gamma_e \leqslant \gamma_c \\[2ex]
\left(\dfrac{\gamma_e}{\gamma_c}\right)^{-(q_e+1)} & \text{for } \gamma_c < \gamma_e < \gamma_{e,2} \\[2ex]
0 & \text{else.}
\end{cases}
\tag{2}
$$

Since radiative cooling depends on a self-consistent radiation field, including synchrotron emission from the present relativistic electron population, an iterative scheme is applied: the code starts out with an equilibrium based on only synchrotron and external Compton (EC) cooling. This distribution is then used to calculate the synchrotron radiation energy density, which is added to the total radiation energy density to re-calculate γ_c and the resulting equilibrium particle distribution. The process is iterated until convergence is achieved.

The code then evaluates the resulting kinetic power in relativistic electrons in the AGN frame,

$$
L_e = \pi R^2 \Gamma^2 \beta_\Gamma \, c \, m_e c^2 \int_1^\infty d\gamma_e \, n_e(\gamma_e) \, \gamma_e
\tag{3}
$$

and compares it to the power carried in the magnetic field (Poynting flux),

$$
L_B = \pi R^2 \Gamma^2 \beta_\Gamma \, c \, \frac{B^2}{8\pi}.
\tag{4}
$$

We define the equipartition parameter as the ratio of the two, i.e., $\epsilon_{Be} \equiv L_B/L_e$. We also evaluate the kinetic luminosity in cold protons that are expected to be present if charge neutrality is provided by one cold proton per electron (i.e., no pairs):

$$
L_p = \pi R^2 \Gamma^2 \beta_\Gamma \, c \, n_e \, m_p c^2.
\tag{5}
$$

The presence of pairs in addition to an electron–proton plasma in the jet will lower the total kinetic luminosity of the jet, $L_{\text{kin}} \equiv L_e + L_p$.

The solid line in Figure 1 shows a generic model blazar SED with an EC component calculated with the full BLR re-processing calculation described in Böttcher & Bloom (2000; dot-dashed line) for a blazar located at a redshift of $z = 0.3$. For this calculation, we assumed a Shakura–Sunyaev accretion disk with a luminosity of $L_D = 10^{45}$ erg s^{-1} with a multi-color blackbody spectrum (the dotted line in Figure 1) peaking at $\nu_D \approx 3.9 \times 10^{14}$ Hz in the AGN rest frame. A spherical BLR with a re-processing fraction $\eta_{\text{BLR}} = 0.04$ is placed at a distance $R_{\text{BLR}} = 0.2$ pc from the accretion disk. The average radiation energy density inside the BLR is commonly estimated as

$$
u_{\text{BLR}} = \frac{L_D \, \eta_{\text{BLR}}}{4\pi \, R_{\text{BLR}}^2 \, c} \approx 2.9 \times 10^{-4} \text{ erg cm}^{-3}.
\tag{6}
$$

In an emission region located close to the inner edge of the BLR, an electron distribution is injected with a power law with index $q = 2.5$ between $\gamma_1 = 10^3$ and $\gamma_2 = 5 \times 10^5$. The equilibrium electron population is in the fast cooling regime.

For comparison, the dashed line in Figure 1 shows the (much faster) calculation of the EC component using an isotropic, thermal radiation field with a blackbody temperature $T = 5000$ K, reproducing a peak energy close to the that of the accretion disk, and with an energy density of $u_{\text{ext}} = 2.5 \times 10^{-4}$ erg cm^{-3}. The figure shows that the isotropic radiation field approximation with these parameters provides an excellent description of the EC component. This indicates that the approximation of Equation (6) slightly overestimates the energy density of the radiation field. In the comprehensive modeling effort described in Section 4, we represent all BLR components as isotropic radiation fields, keeping in mind that a simple translation of disk and BLR parameters to the external radiation field energy density of Equation (6) needs to be taken with caution.

The model described above has already been used successfully to model a number of blazar SEDs. In particular, it has been used to interpret the SEDs of blazars detected in VHEs ($E > 100$ GeV) by VERITAS, e.g., W Comae (Acciari et al. 2008, 2009b), 1ES 0806+524

(Acciari et al. 2009a), PKS 1424+240 (Acciari et al. 2010a), RGB J0710+591 (Acciari et al. 2010b), and 3C 66A (Abdo et al. 2011). It has also been used to model the SED of the high-redshift FSRQ PKS 0528+134 in quiescence (Palma et al. 2011).

3. STATIONARY HADRONIC BLAZAR MODEL

In order for protons to contribute significantly to the radiative output in relativistic jets of blazars either through proton-synchrotron emission (Aharonian 2000; Mücke & Protheroe 2000) or photo-pion production (Mannheim & Biermann 1992), they need to be accelerated to proton energies of typically $E_p \equiv E_{19} 10^{19}$ eV with $E_{19} \gtrsim 1$. Requiring that the Larmor radius of these protons be smaller than the size of the emission region, $R \equiv 10^{15} R_{15}$ cm, one needs magnetic fields of $B \geqslant 30 E_{19} R_{15}^{-1}$ G. The energy density of such large magnetic fields is likely to dominate over the energy density of external radiation fields in typical AGN environments so that the synchrotron radiation field is likely to be the dominant target photon field for photo-pion production by ultrarelativistic protons. We will therefore restrict our considerations in this paper to the synchrotron-proton blazar (SPB) model as discussed in detail in Mücke & Protheroe (2001) and Mücke et al. (2003).

For a comparison between leptonic and hadronic blazar models on the basis of a sufficiently large sample, we need a hadronic model implementation that allows for efficient scanning through parameter space within a reasonable time frame. At the same time, the model needs to treat hadronic processes to a degree of detail comparable to the leptonic processes being considered in the leptonic model described in the previous section. The most accurate and reliable method to evaluate the radiative output from photo-pair and photo-pion production and the cascades initiated by $\gamma\gamma$ absorption of ultrahigh energy (UHE; $E \gg 1$ TeV) photons produced through π^0 decay and synchrotron emission of pions and their decay products, is through Monte Carlo simulations (e.g., Mücke et al. 2000a). However, such simulations are quite time consuming, and a comprehensive modeling effort of a large sample of SEDs is currently infeasible with this method.

In order to avoid time-consuming Monte Carlo simulations, Kelner & Aharonian (2008) have developed analytical expressions for the final decay products (electrons, positrons, photons, and neutrinos) from photo-pion production for isotropically distributed, monoenergetic photons and protons. These can be integrated over any proton and photon distribution to obtain the final production spectra of electrons, positrons, photons, and neutrinos. However, the π^0 decay photons as well as synchrotron photons from these first-generation electrons and positrons emerge in the UHE regime, at which the dense radiation fields in the emission regions of blazars are highly opaque to $\gamma\gamma$ pair production. It is therefore essential to include the effects of UHE γ-ray induced pair cascades in hadronic models. Again, time-consuming Monte Carlo/numerical simulations constitute the standard method for the evaluation of such cascades.

3.1. Synchrotron-supported Pair Cascades

For the purpose of an efficient calculation of cascades, we have developed a semianalytical method that does not involve Monte Carlo simulations. Let us assume that the injection rates of first-generation high-energy γ-rays, $\dot{N}_\epsilon^0$, and pairs, $Q_e(\gamma)$, are known, e.g., from the analytical approximations of Kelner

& Aharonian (2008). Throughout this exposition, we use the dimensionless photon energy $\epsilon \equiv h\nu/m_e c^2$. In the case of linear cascades, the optical depth for $\gamma\gamma$ absorption, $\tau_{\gamma\gamma}(\epsilon)$ can be pre-calculated from the low-energy radiation field. Under these conditions, the spectrum of escaping (observable) photons can be calculated as

$$\dot{N}_\epsilon^{\mathrm{esc}} = \dot{N}_\epsilon^{\mathrm{em}} \left(\frac{1 - e^{-\tau_{\gamma\gamma}[\epsilon]}}{\tau_{\gamma\gamma}[\epsilon]} \right), \qquad (7)$$

where $\dot{N}_\epsilon^{\mathrm{em}}$ has contributions from the first-generation high-energy photon spectrum and synchrotron emission from secondaries, $\dot{N}_\epsilon^{\mathrm{em}} = \dot{N}_\epsilon^0 + \dot{N}_\epsilon^{\mathrm{sy}}$. We use a synchrotron emissivity function for a single electron of the form $j_\nu \propto \nu^{1/3} e^{-\epsilon/\epsilon_0}$ with $\epsilon_0 = b\gamma^2$, where $b \equiv B/B_{\mathrm{crit}}$ and $B_{\mathrm{crit}} = 4.4 \times 10^{13}$ G. This yields

$$\dot{N}_\epsilon^{\mathrm{sy}} = A_0 \, \epsilon^{-2/3} \int_1^\infty d\gamma \, N_e(\gamma) \, \gamma^{-2/3} \, e^{-\epsilon/(b\gamma^2)} \qquad (8)$$

with the normalization

$$A_0 = \frac{c \, \sigma_T \, B^2}{6\pi \, m_e c^2 \, \Gamma(4/3) \, b^{4/3}}. \qquad (9)$$

The electron distribution, $N_e(\gamma)$, will be the solution to the isotropic Fokker–Planck equation in equilibrium ($\partial\langle.\rangle/\partial t = 0$):

$$\frac{\partial}{\partial\gamma} (\dot{\gamma} \, N_e[\gamma]) = Q_e(\gamma) + \dot{N}_e^{\gamma\gamma}(\gamma) + \dot{N}_e(\gamma)^{\mathrm{esc}}. \qquad (10)$$

In the case under consideration here, the electron energy losses will be dominated by synchrotron losses, i.e.,

$$\dot{\gamma} = -\frac{c \, \sigma_T \, B^2}{6\pi \, m_e c^2} \, \gamma^2 \equiv -\nu_0 \gamma^2. \qquad (11)$$

We represent the escape term in Equation (10) through an energy-independent escape timescale $t_{\mathrm{esc}} = \eta_{\mathrm{esc}} R/c$, so that $\dot{N}_e(\gamma)^{\mathrm{esc}} = -N_e(\gamma)/t_{\mathrm{esc}}$. $\dot{N}_e^{\gamma\gamma}(\gamma)$ in Equation (10) is the rate of particle injection due to $\gamma\gamma$ absorption to be evaluated self-consistently with the radiation field. In the $\gamma\gamma$ absorption of a high-energy photon of energy ϵ, one of the produced particles will assume the major fraction, f_γ of the photon energy. From a comparison with Monte Carlo simulations, we find that $f_\gamma = 0.9$ yields good agreement with numerical solutions to the cascade problem. Hence, an electron/positron pair with energies $\gamma_1 = f_\gamma \epsilon$ and $\gamma_2 = (1 - f_\gamma) \epsilon$ is produced. Furthermore, realizing that every photon not escaping (according to Equation (7)) will produce an electron/positron pair, we can write the pair production rate as

$$\dot{N}_e^{\gamma\gamma}(\gamma) = f_{\mathrm{abs}}(\epsilon_1) \left(\dot{N}_{\epsilon_1}^0 + \dot{N}_{\epsilon_1}^{\mathrm{sy}} \right) + f_{\mathrm{abs}}(\epsilon_2) \left(\dot{N}_{\epsilon_2}^0 + \dot{N}_{\epsilon_2}^{\mathrm{sy}} \right), \quad (12)$$

where $\epsilon_1 = \gamma/f_\gamma$, $\epsilon_2 = \gamma/(1 - f_\gamma)$ and

$$f_{\mathrm{abs}}(\epsilon) \equiv 1 - \frac{1 - e^{-\tau_{\gamma\gamma}(\epsilon)}}{\tau_{\gamma\gamma}(\epsilon)}. \qquad (13)$$

With this approximation, we find an implicit solution to Equation (10)

$$N_e(\gamma) = \frac{1}{\nu_0 \gamma^2} \int_\gamma^\infty d\tilde{\gamma} \left\{ Q_e(\tilde{\gamma}) + \dot{N}_e^{\gamma\gamma}(\tilde{\gamma}) - \frac{N_e(\tilde{\gamma})}{t_{\mathrm{esc}}} \right\}. \quad (14)$$
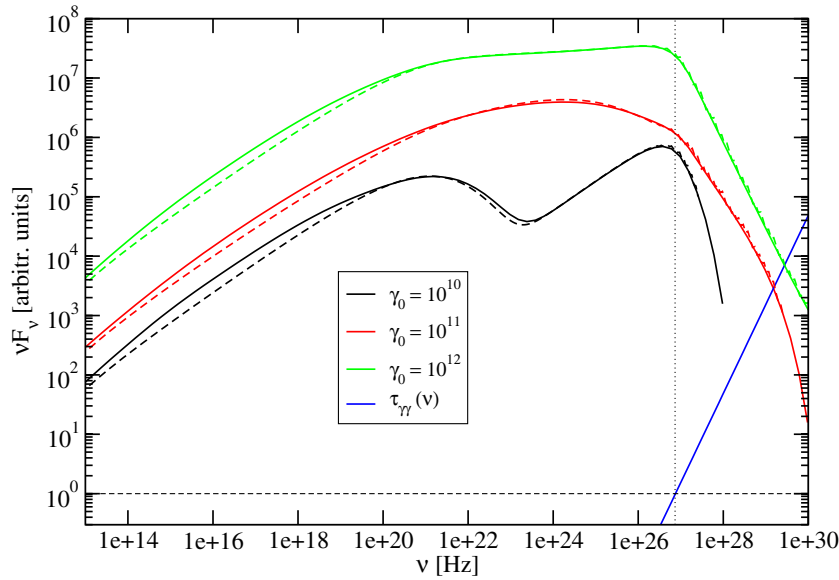
Figure 2. Comparison of the cascade emission from Monte Carlo simulations (solid curves) and our semianalytical description (dashed curves) in the case of the injection of monoenergetic electrons with energies given by the labels in a $B = 10$ G magnetic field. The blue curve shows the $\gamma\gamma$ opacity as a function of γ-ray photon frequency.

(A color version of this figure is available in the online journal.)

The solution (Equation 14) is implicit in the sense that the particle spectrum $N_e(\gamma)$ occurs on both sides of the equation as $\dot{N}_e^{\gamma\gamma}$ depends on the synchrotron emissivity calculated through Equation (8), which requires knowledge of $N_e(\tilde{\gamma})$, where pairs at energies of $\tilde{\gamma}_1 = \sqrt{\gamma/(f_\gamma b)}$ and $\tilde{\gamma}_2 = \sqrt{\gamma/([1 - f_\gamma] b)}$ provide the majority of the radiative output relevant for pair production at energy γ. However, for practical applications, we may use the fact that generally, γ, the argument on the left-hand side, is much smaller than $\tilde{\gamma}_{1,2}$. Therefore, Equation (14) may be evaluated progressively, starting at the highest pair energies for which $Q_0(\gamma) \neq 0$ or $\dot{N}_{\epsilon_{1,2}}^0 \neq 0$, and then using the solution for $N_e(\gamma)$ for large γ as one progresses toward lower values of γ.

Once the equilibrium pair distribution $N_e(\gamma)$ is known, it can be used in Equation (8) to evaluate the synchrotron emissivity, and hence using Equation (7) the observable photon spectrum.

Figure 2 illustrates the Monte Carlo generated synchrotron + cascade spectra (solid lines) for the injection of monoenergetic electrons with energies $\gamma_0 = 10^{10}$, 10^{11}, and 10^{12}, respectively. The magnetic field is $B = 10$ G, and the $\gamma\gamma$ optical depth as a function of photon energy is shown by the blue solid curve. The dashed lines illustrate the results of the analytic approximations developed here. The agreement between Monte Carlo simulations and the semianalytic approximation is excellent, especially throughout the γ-ray regime. At lower energies, our approximation remains accurate to within a factor of $\lesssim 2$.

3.2. Proton Energy Losses and Equilibrium Particle Distribution

In addition to the π^0 and electron/proton-synchrotron cascades, proton-synchrotron emission is the other main contributor to the high-energy emission in hadronic models (Mücke & Protheroe 2000; Aharonian 2000). In our model, we use an asymptotic approximation analogous to Equation (8) for the proton-synchrotron emissivity.

An equilibrium proton distribution is evaluated assuming the injection of a power-law distribution of protons, $Q_p(\gamma_p) = Q_{0,p} \gamma_p^{-q_p} H(\gamma_p; \gamma_{1,p}, \gamma_{2,p})$. As in the leptonic model described

in Section 2, a self-consistent equilibrium between this injection, particle escape, and cooling is evaluated. Unlike the case of electrons, radiative cooling timescales for protons can be longer than the typical dynamical timescale of the expansion of the emission region. We therefore account for adiabatic energy losses as well as radiative energy losses for the protons.

Adiabatic losses are evaluated through $\dot{\gamma}_p/\gamma_p = -\dot{V}/V$, where V is the volume of the emission region. Assuming a conical jet with opening angle $\theta_j \sim 1/\Gamma$, the adiabatic cooling rate is $\dot{\gamma}_p = -3 c \theta_j \gamma_p/R$. The proton-synchrotron cooling rate is

$$\dot{\gamma}_{p,sy} = -\frac{c \sigma_T B^2}{6\pi m_e c^2} \left(\frac{m_e}{m_p}\right)^3 \gamma_p^2 \qquad (15)$$

and the photo-pion energy losses are approximated as (Aharonian 2000)

$$\dot{\gamma}_{p,p\gamma} = -c \langle \sigma_{p\gamma} f \rangle n_{\text{ph}}(\epsilon^*) \epsilon^* \gamma_p, \qquad (16)$$

where $\langle \sigma_{p\gamma} f \rangle \approx 10^{-28}$ cm^2 is the elasticity-weighted $p\gamma$ interaction cross section and $\epsilon^* = 5.9 \times 10^{-8} E_{19}^{-1}$ is the energy of target photons interacting with protons of energy E at the Δ resonance, which, for plausible blazar parameters, is usually the most relevant contribution to the $p\gamma$ cross section (Mücke et al. 2000b).

The equilibrium proton distribution can then be found by integrating the analog of the isotropic Fokker–Planck equation (10), neglecting particle escape (which only affects the lowest-energy protons which do not substantially contribute to the radiative output):

$$N_p(\gamma_p) = \frac{-1}{\dot{\gamma}_p} \int_\gamma^\infty d\tilde{\gamma}_p \, Q_p(\tilde{\gamma}_p). \qquad (17)$$

In conical jet geometries, the energy loss rates of relativistic protons can conceivably be dominated by adiabatic losses (see, e.g., Sikora 2011). Because of their linear dependence on γ_p, adiabatic losses will not produce a break in the equilibrium
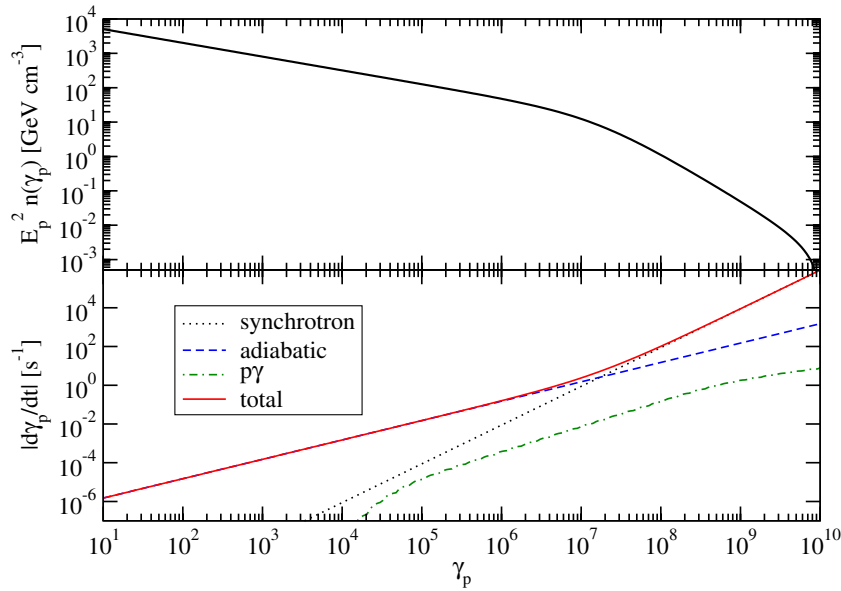
Figure 3. Proton cooling rates (bottom panel) and the equilibrium proton distribution (top panel) evaluated according to Equation (17) for typical proton-synchrotron blazar model parameters (see the text for details).

(A color version of this figure is available in the online journal.)

proton spectrum. Equation (17) predicts a break in the proton spectrum only where radiative (proton synchroton or photo-pion production) losses become dominant. Figure 3 illustrates this effect. The bottom panel shows the proton energy loss rates due to adiabatic, synchrotron, and photo-pion losses, along with the total cooling rate. The target photon field is dominated by synchrotron emission from an electron population injected between $\gamma_{e,1} = 10^3$ and $\gamma_{e,2} = 10^5$ with $q_e = 2.6$, in a magnetic field of $B = 30$ G. Protons were injected with a power-law distribution of index $q_p = 2.4$, between $E_{p,1} = 1$ GeV and $E_{p,2} = 10^{10}$ GeV. The emission region has a radius of $R = 10^{16}$ cm and expands at an angle of $\theta_j = 1/\Gamma$ for $\Gamma = 20$. For these parameters, radiative losses (dominated by proton synchrotron) begin to dominate over adiabatic losses at $\gamma_{p,b} \sim 2 \times 10^7$. While for all proton Lorentz factors, the cooling timescale is shorter than the escape timescale, a break in the equilibrium proton distribution (from index 2.4 to 3.4) occurs only at $\gamma_{p,b}$.

The leptonic component of our hadronic jet model is being handled with the same procedure as described in Section 2 for our leptonic model. The full leptonic radiative output (synchrotron + SSC) is used as the target photon field for photo-pion production of the hadronic component and for evaluating the $\gamma\gamma$ opacity of the emission region.

3.3. Limitations

The Kelner & Aharonian (2008) templates we are using to evaluate the production spectra of the final decay products neglect the synchrotron (and Compton) emission from intermediate decay products, i.e., muons and pions. It has been shown (Mücke et al. 2003) that under certain conditions, these emissions can make a non-negligible contribution to the high-energy spectra in the SPB model. Neglecting these contributions is acceptable if one of two conditions is fulfilled: (1) the synchrotron cooling timescale of relativistic muons and pions are much longer than their decay timescales or (2) proton-synchrotron losses strongly dominate over photo-pion losses.

For condition (1), we need to compare the decay timescales of pions (muons) with Lorentz factors γ_π (γ_μ) in the blob rest frame,

$$t_d^\pi = 2.6 \times 10^{-8}\, \gamma_\pi \text{ s}$$
$$t_d^\mu = 2.2 \times 10^{-6}\, \gamma_\mu \text{ s,} \tag{18}$$

to the pion (muon) synchrotron cooling timescale analogous to Equation (15). This yields the conditions

$$B\,\gamma_p \ll \begin{cases} 7.8 \times 10^{11} \text{ G} & \text{for pions} \\ 5.6 \times 10^{10} \text{ G} & \text{for muons.} \end{cases} \tag{19}$$

The Lorentz factors of secondary pions and muons are of the order of the Lorentz factors of the primary protons. Therefore, Equation (19) constitutes a restriction to the highest proton Lorentz factors allowed for a given magnetic field so that pion and muon synchrotron emission can be neglected. Obviously, the condition is more restrictive for muons than for pions. Our code automatically prints out a warning if condition (19) is not fulfilled for either muons or pions.

To check for condition (2), i.e., proton-synchrotron losses being dominant over photo-pion losses, our code evaluates the proton-synchrotron and photo-pion energy loss rates automatically (as plotted, for example, in Figure 3). We only trust our results if either condition (1) for muons or condition (2) is fulfilled. Specifically, this means that our semianalytical hadronic model is not applicable to situations with both very high magnetic fields and high radiation energy densities, in which photo-pion production may dominate over proton-synchrotron emission, and the synchrotron cooling timescales of muons (and pions) may be shorter than their decay timescale.

In summary, our steady-state hadronic emission model is limited by its neglect of pion and muon synchrotron radiation, implying restrictions to the maximum possible field strength as a function of maximum proton energy injected. Protons may lose their energy radiatively either via the proton-synchrotron channel or photomeson production. If the latter is the case, Bethe–Heitler pair production is considered subdominant, and

Table 1
Observational Data Used to Constrain Our Models

Object Name	Type	z	$\beta_{\perp,app}$	t_{var}	L_{disk} (erg s^{-1})	L_{BLR} (erg s^{-1})
3C 273	FSRQ	0.158	13 [1]	1 d [2]	1.3×10^{47} [3]	9.1×10^{45} [4]
3C 279	FSRQ	0.536	20.6 [5]	2 d [6]	2.0×10^{45} [7]	2.0×10^{44} [8]
3C 454.3	FSRQ	0.859	14.9 [5]	1 hr [9]	1.7×10^{47} [10]	2.5×10^{45} [11]
PKS 1510−089	FSRQ	0.36	20.3 [5]	1 d [12]	1.0×10^{46} [13]	⋯
PKS 0420−01	FSRQ	0.916	7.5 [5]	4 d [14]	1.5×10^{46} [11]	4.3×10^{44} [11]
PKS 0528+134	FSRQ	2.06	30 [15]	1 d [16]	1.7×10^{47} [16]	1.8×10^{46} [16]
BL Lacertae	LBL	0.069	10.7 [5]	1.5 hr [17]	6.0×10^{44} [18]	6.3×10^{42} [11]
AO 0235+164	LBL	0.94	2 [5]	1.5 d [19]	3.4×10^{44} [11]	3.7×10^{43} [11]
S5 0716+714	LBL	0.31	10.2 [5]	15 min [20]	⋯	⋯
OJ 287	LBL	0.306	15.3 [5]	2 hr [21]	1.1×10^{45} [11]	2.7×10^{43} [11]
W Comae	IBL	0.102	2 [22]	5 hr [23]	7.2×10^{44} [11]	5.0×10^{41} [11]
3C 66A	IBL	0.44 ?	27 [24]	6 hr [25]	⋯	⋯

Notes. Superscripts in parantheses refer to the following references: (1) Lister et al. 2009; (2) Courvoisier et al. 1988; (3) Vasudevan & Fabian 2009; (4) Peterson et al. 2004; (5) Hovatta et al. 2009; (6) Böttcher et al. 2007; (7) Hartman et al. 2001; (8) Pian et al. 2005; (9) Raiteri et al. 2008a; (10) Raiteri et al. 2008c; (11) Xie et al. 2008; (12) Marscher et al. 2010; (13) Pucella et al. 2008; (14) D'Arcangelo et al. 2007; (15) Jorstad et al. 2005; (16) Palma et al. 2011; (17) Villata et al. 2002; (18) Raiteri et al. 2009; (19) Raiteri et al. 2008b; (20) Sasada et al. 2008; (21) Fan et al. 2009; (22) Massaro et al. 2001; (23) Tagliaferri et al. 2000; (24) Jorstad et al. 2001; (25) Takalo et al. 1996.

is therefore neglected. The high-energy photons and secondary particles from photomeson production may initiate cascades where the injected power is redistributed by means of synchrotron radiation. We restrict ourselves to linear cascades. Inverse Compton losses are neglected owing to the large magnetic field strengths in the emission region considered here.

External radiation fields as the target field for particle and photon interactions and cascading are also not considered here. We point out that in the case of FSRQs, this simplification may not always be justified (e.g., Atoyan & Dermer 2003). We have therefore carefully verified whether the external radiation fields in the six FSRQs modeled in this paper (see Section 4) may make a substantial contribution to the target photon fields for pion production. For most of them, the comoving synchrotron-photon energy density in our hadronic model is at least two orders of magnitude larger than the comoving-frame energy density of the external radiation field used for the leptonic models (which were based on the observed BLR luminosity and a typical size of the BLR). Direct accretion disk emission is unlikely to play a non-negligible role due to the unfavorable angle of incidence, which requires very high proton Lorentz factors for photo-pion production, as would the interaction with an infrared radiation field from a dust torus. However, for 3C454.3 and PKS 0528+134, we find that the BLR radiation field (Doppler-boosted into the comoving frame) may be of the order of or even larger than the synchrotron-photon energy density, depending on the (unknown) radius of the BLR and the location of the γ-ray emitting region with respect to the BLR. We therefore caution that our neglect of external radiation fields may not be valid in those two cases.

4. COMPARATIVE MODELING OF *FERMI*-LAT-DETECTED BLAZARS

In this section, we will apply our leptonic and hadronic models described in the previous sections to a set of γ-ray blazars detected by *Fermi*-LAT. Abdo et al. (2010) presented a comprehensive compilation of simultaneous or contemporaneous broadband SEDs of a large sample of *Fermi*-LAT-detected blazars. Out of their list, we selected a subset of blazars which fulfilled the following criteria: (1) good simultaneous broad-

band SED coverage, including at least optical/IR, X-ray, and γ-ray data; (2) known redshift; (3) information about short-term variability; (4) apparent superluminal motion; (5) in the case of FSRQs information about the accretion disk and BLR luminosity. Condition (1) is necessary to allow for meaningful SED fitting. Condition (2) is required to determine the overall luminosity requirements of models. Condition (3) allows us to derive constraints on the size of the emission region from the observed variability timescale t_{var} via $R \leqslant Dct_{var}/(1 + z)$; (4) superluminal motion with a speed $\beta_{\perp,app}$ allows us to place a lower limit on the bulk Lorentz factor of $\Gamma \geqslant \sqrt{\beta_{\perp,app}^2 + 1}$; and (5) knowledge of the accretion disk and BLR luminosities further constrains the modeling of FSRQs in which these sources of external radiation fields are generally believed to be important.

We found that the following objects fulfilled our criteria: the FSRQs 3C 273, 3C 279, 3C 454.3, PKS 1510−089, PKS 0420−01, and PKS 0528+134; the LBLs BL Lacertae, AO 0235+164, S5 0716+714, and OJ 287; and the IBLs W Comae and 3C 66A. SED data for these objects are obtained from Abdo et al. (2010), and Table 1 lists observational data that are used to further constrain our models.

Our fitting procedure is a "fit-by-eye" method, starting with plausible values for the parameters that are not directly constrained by observations. The unconstrained parameters are then adjusted to obtain an acceptable representation of the SED. Simpler models with fewer parameters, such as a single-zone, static SSC model, allow for a detailed χ^2 minimization technique (see, e.g., Mankuzhiyil et al. 2011). However, given the substantial number of adjustable parameters, such a fitting method is infeasible for the models considered here. While we are confident that our best-fit parameters are in the correct ball-park range for these objects, the lack of a rigorous χ^2 minimization strategy prevents us from determining errors on the fit parameters. Therefore, while we will proceed to a global assessment of parameter values among different classes of blazars, we will refrain from any quantitative statements in this respect.

In the course of the fitting, we strive to achieve acceptable fits with parameters close to equipartition between the dominant particle species (electrons in the leptonic model and protons in

Table 2
Parameters for the Leptonic SED Fits Shown in Figures 4–6

Object	$\gamma_{e,1}$	$\gamma_{e,2}$	q_e	B [G]	D	f_{BLR}[a]	L_e[b]	L_p[b]	L_B[b]	ϵ_{Be}	$t_{var,min}$[c]
3C 273	1×10^3	5×10^4	3.5	2.0	13	5.4×10^{-5}	6.0	130	0.63	0.11	4.1
3C 279	1×10^3	1×10^5	3.0	0.7	17	1.7×10^{-2}	5.8	29	5.4	0.94	29
3C 454.3	800	5×10^4	3.0	2.1	15	8.0×10^{-2}	22	870	75	3.5	52
PKS 1510−089	1×10^3	2×10^5	3.1	0.8	20	4.1×10^{-3}	2.1	41	2.1	1.0	9.4
PKS 0420−01	1.4×10^3	5×10^4	3.4	2.5	8.0	1.0×10^{-1}	6.9	670	38	5.4	110
PKS 0528+134	700	1×10^4	3.0	3.0	19	9.1×10^{-3}	9.4	600	110	11	45
BL Lacertae	1.1×10^3	1×10^5	3.2	2.5	15	1.3×10^{-1}	0.44	4.6	0.41	0.94	1.8
AO 0235+164	700	5×10^4	3.7	1.3	25	1.1	12	87	33	2.8	21
S5 0716+714	1.9×10^3	5.5×10^4	3.8	3.8	20	. . . [d]	1.3	6.7	14	10	4.9
OJ 287	800	5×10^4	3.8	3.5	15	1.5×10^{-1}	1.8	16	15	8.2	9.7
W Comae	1×10^3	8×10^4	2.4	1.5	30	2.8×10^{-2}	0.30	1.52	0.30	1.0	0.68
3C 66A	9×10^3	3×10^5	2.8	0.065	40	. . . [d]	13	8.2	0.45	0.034	13

Notes.
[a] The factor f_{BLR}, determining the energy density of the re-processed disk radiation field, is defined as $f_{BLR} \equiv \eta_{BLR}/R_{BLR}^2$; values are in pc^{-2}.
[b] Powers are in units of 10^{44} erg s^{-1}.
[c] Minimum allowed variability timescale in hours.
[d] For S5 0716+714 and 3C 66A, no accretion disk luminosity has been measured/constrained; for S5 0716+714, an isotropic external radiation field with $u_{ext} = 5 \times 10^{-5}$ erg cm^{-3} and $T_{BB} = 2 \times 10^4$ K has been used for the SED fit; for 3C 66A: $u_{ext} = 1.3 \times 10^{-8}$ erg cm^{-3} and $T_{BB} = 10^3$ K.

the hadronic model) and the magnetic field. This is motivated by two arguments: (1) if the relativistic jets of AGNs are powered by rotational energy from the central black hole (Blandford & Znajek 1977), the jets are expected to be initially Poynting-flux-dominated, and the energy carried in electromagnetic fields needs to be transferred to relativistic particles in order to produce the observed high-energy emission. This energy conversion is expected to cease as approximate equipartition between the magnetic field and relativistic particles is reached, so that the jets are not expected to become matter-dominated in the central few parsecs of the AGN, where the high-energy emission in blazars is believed to be produced (Lyubarsky 2010). (2) If magnetic pressure plays an essential role in collimating AGN jets out to kiloparsec scales, the particle pressure cannot largely dominate over the magnetic pressure in the inner few parsecs of the AGN. For these reasons, we prefer model parameters with magnetic fields dominating the pressure and energy density in the emission region over particle-dominated scenarios.

For all objects, we produced one leptonic and one hadronic model fit to the contemporaneous SED. In the case of 3C 66A, the catalog value of the redshift of $z = 0.444$ is highly questionable. The recent analyses of Prandini et al. (2010) and Abdo et al. (2011) place the object at a likely redshift of $z \sim 0.2$–0.3, while Furniss et al. (2013) provide a lower limit on the redshift of $z \geqslant 0.3347$, based on UV absorption features of the intervening intergalactic medium. In our modeling, we assume a fiducial redshift of $z = 0.3$ for 3C 66A. While, of course, the parameter values slightly change when using a slightly higher redshift (say, $z = 0.35$ to be consistent with Furniss et al. 2013), the overall conclusions from the modeling remain unaffected. All our model SEDs are corrected for $\gamma\gamma$ absorption by the extragalactic background light using the model of Finke et al. (2010).

4.1. Leptonic Model Fits

Figures 4–6 show the SEDs and our leptonic model fits for the 12 blazars we selected for this study. The fit parameters used and a few quantities derived from those parameters, are listed in Table 2. In general, satisfactory fits to most blazar SEDs with parameters close to (within an order of magnitude of)

equipartition can be achieved with the leptonic model described above.

In agreement with many previous studies, we find that FSRQs require a dominant contribution from EC (on the direct accretion disk and the BLR emission) in order to provide acceptable SED fits (e.g., Sambruna et al. 1997; Ghisellini et al. 1998; Mukherjee et al. 1999; Hartman et al. 2001). In our model fits, we are able to produce the spectral breaks observed in the *Fermi*-LAT spectra of many blazars, with a superposition of two different γ-ray emission components, as previously proposed for the case of 3C454.3 by Finke & Dermer (2010). Typical minimum variability timescales from light-travel time arguments are of the order of 1–2 days, consistent with the day-scale variability seen in most *Fermi*-detected FSRQs.

As argued previously, e.g., by Madejski et al. (1999) and Böttcher & Bloom (2000) for the case of BL Lacertae, LBLs are also represented with more plausible parameters when including an EC component using a low-luminosity accretion disk and BLR compared to a pure SSC model. In the case of S5 0716+714, where no observationally motivated estimates of the luminosity of the accretion disk or the BLR could be found, we have assumed the existence of a dust torus with a very low infrared luminosity, consistent with the absence of any direct observational evidence for it. Our models allow for variability on timescales of a few hours for the LBLs modeled here. While the SEDs of BL Lacertae objects, S5 0716+714 and OJ 287, are well represented by a leptonic SSC+EC model, our model has problems representing the very hard γ-ray spectrum of AO 0235+164 above a few GeV as our model γ-ray spectra are truncated by Klein–Nishina effects.

In blazars in which we find that a substantial contribution from EC on direct accretion disk emission is relevant, we find a best-fit distance of the γ-ray emission region from the central black hole in the range $z_0 \lesssim 0.1$ pc. An important contribution from EC on BLR emission would imply a characteristic distance of $z \lesssim 1$ pc, while a much larger distance would be consistent with situations in which EC on infrared emission (from warm dust) dominates the γ-ray production. As described in Section 2, the external radiation fields from the BLR and/or warm dust are modeled as isotropic in the AGN rest frame so that for such fits,
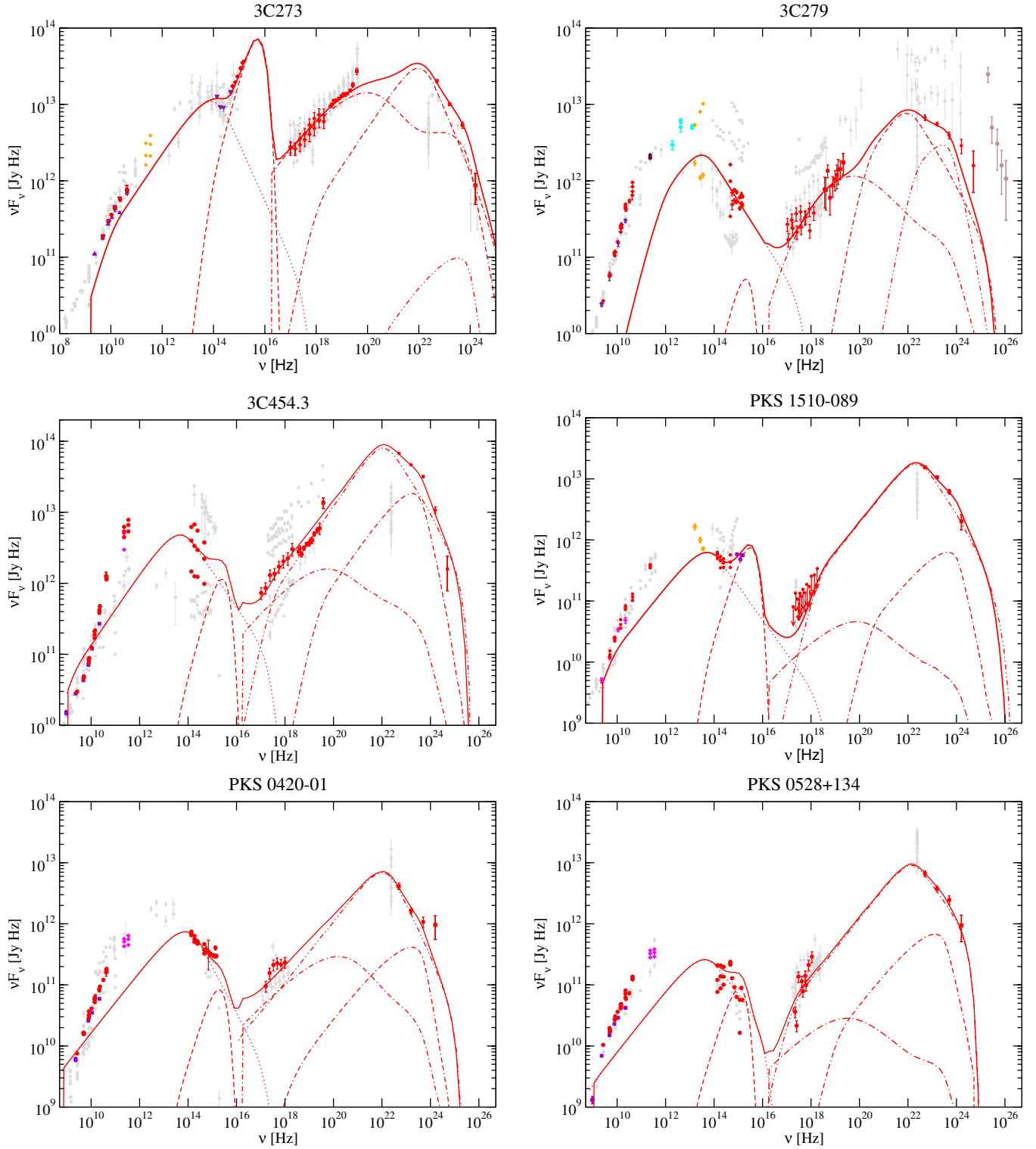
Figure 4. Leptonic model fits to the six FSRQs in our sample. See Table 2 for parameters. Dotted: synchrotron; dashed: accretion disk; dot-dashed: SSC; dot-dash-dashed: EC (disk); dot-dot-dashed: EC (BLR).

(A color version of this figure is available in the online journal.)

the distance to the black hole is not a necessary input parameter for our model.

While BL Lac objects detected at >100 GeV γ-rays by ground-based Atmospheric Cherenkov Telescopes have often been found to be well represented by pure SSC models, the careful analysis of the simultaneous SEDs of the VERITAS-detected IBLs W Comae and 3C 66A (Acciari et al. 2009b;

Abdo et al. 2011) revealed that also in these two cases, a pure SSC fit would require rather extreme parameters with magnetic fields far below equipartition. This situation could be remedied allowing for a contribution from EC to the γ-ray emission. These findings are confirmed in this study. However, the unusual, apparent upward curvature of the *Fermi*-LAT spectrum of 3C 66A and W Comae cannot be satisfactorily represented with
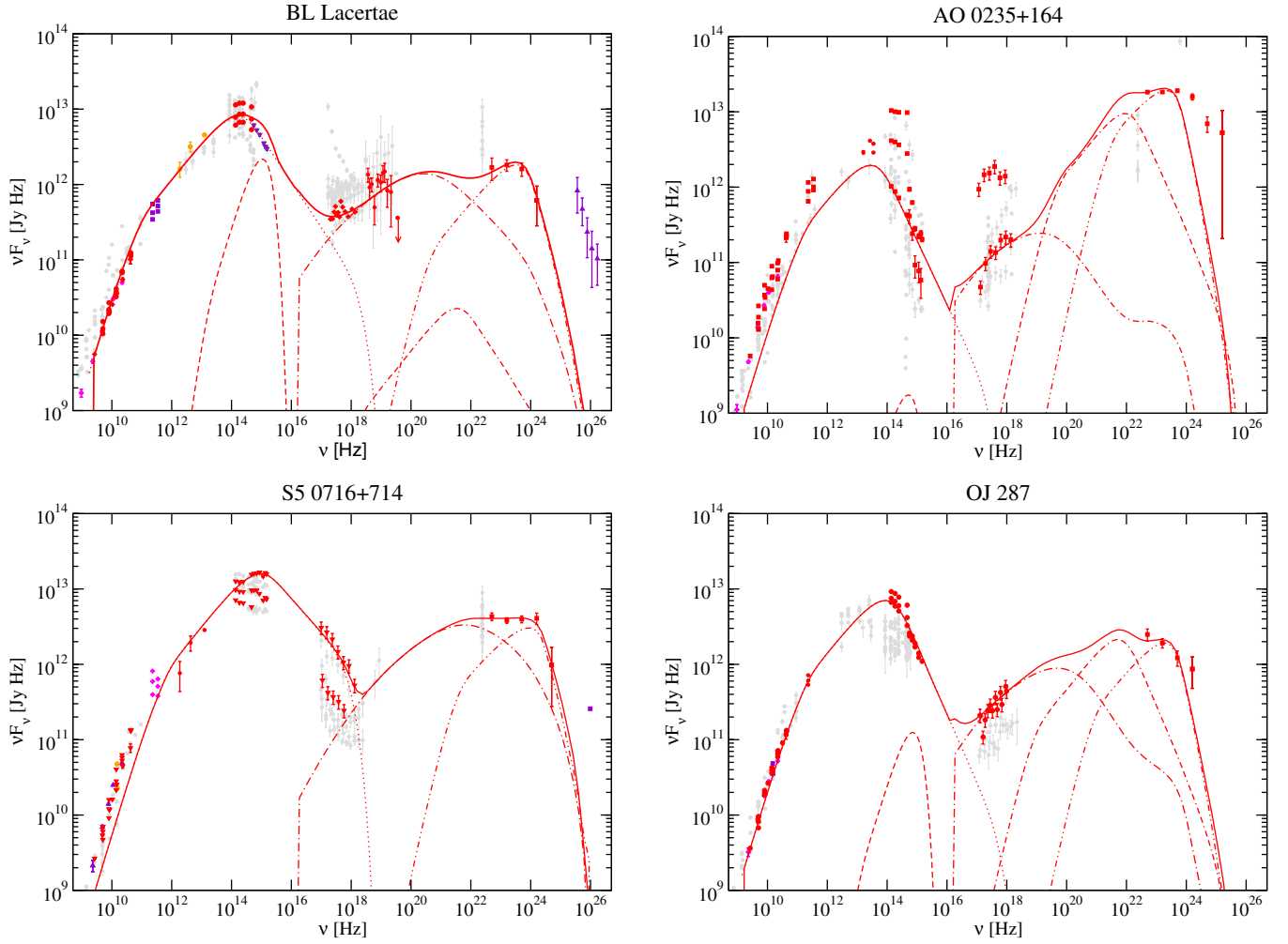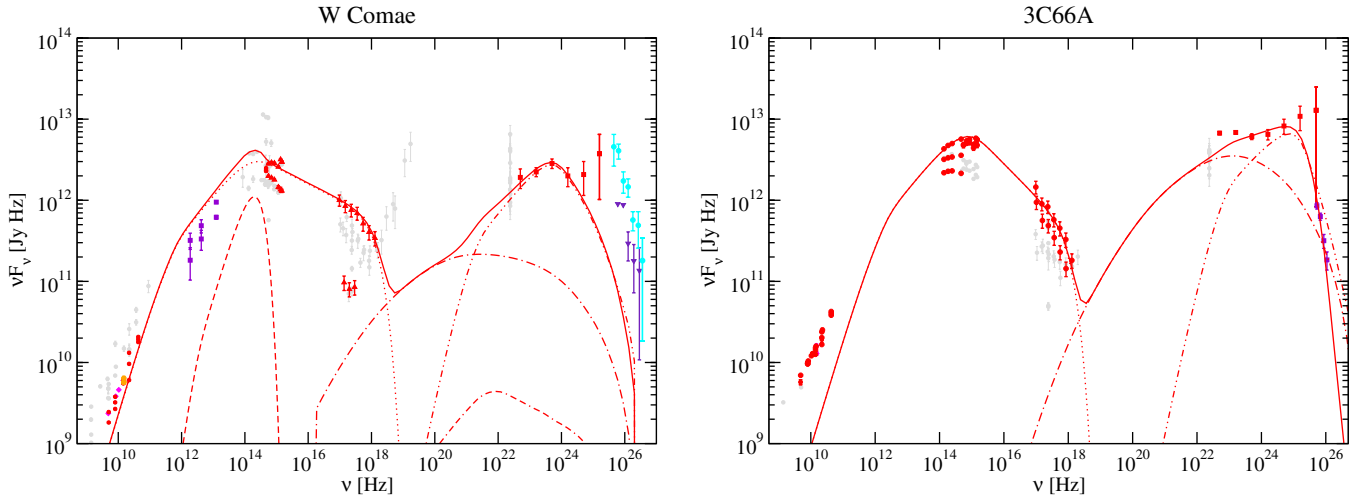
Figure 5. Leptonic model fits to the four LBLs in our sample. See Table 2 for parameters. Dotted: synchrotron; dashed: accretion disk; dot-dashed: SSC; dot-dash-dashed: EC (disk); dot-dot-dashed: EC (BLR).

(A color version of this figure is available in the online journal.)

Figure 6. Leptonic model fits to the two IBLs in our sample. See Table 2 for parameters. Dotted: synchrotron; dashed: accretion disk; dot-dashed: SSC; dot-dash-dashed: EC (disk); dot-dot-dashed: EC (BLR).

(A color version of this figure is available in the online journal.)

our model, irrespective of the dominant target photon field for external Compton scattering.

We find that the two IBLs in our sample require systematically higher Doppler factors than the LBLs and FSRQs. Also, as

expected, BL Lac objects are characterized by less powerful jets (i.e., lower L_e) than FSRQs, and the two IBLs require harder electron spectra than the LBLs and FSRQs. We do not find a systematic difference in magnetic field values between BL Lac

Table 3
Parameters for the Hadronic SED Fits Shown in Figures 7–9

Object	$\gamma_{e,1}$	$\gamma_{e,2}$	q_e	B[a]	D	$\gamma_{p,max}$	q_p	L_e[b]	L_p[c]	ϵ_{Be}[d]	ϵ_{Bp}[d]	ϵ_{ep}[d]	t_{var}[e]
3C 273	350	1.5×10^4	3.4	15	15	4.3×10^8	2.4	0.13	25	3300	1.7×10^{-3}	5.2×10^{-7}	11
3C 279	100	2.0×10^4	3.0	100	15	6.4×10^8	2.2	0.19	3.5	1410	7.9×10^{-3}	5.6×10^{-6}	1.7
3C 454.3	300	1.5×10^4	3.2	10	15	1.1×10^9	2.1	1.0	35	1.2×10^4	0.035	2.9×10^{-6}	138
PKS 1510−089	150	1.5×10^4	3.2	10	20	1.1×10^9	1.7	0.57	2.5	24	5.4×10^{-4}	2.3×10^{-5}	1.9
PKS 0420−01	75	1.0×10^4	3.2	100	10	4.3×10^8	1.3	0.52	0.42	2200	0.27	1.2×10^{-4}	9.7
PKS 0528+134	150	1.0×10^4	3.8	30	20	1.1×10^9	2.0	1.9	44	1020	4.4×10^{-3}	4.3×10^{-6}	17
BL Lacertae	700	1.5×10^4	3.5	10	15	1.9×10^9	2.4	0.087	9.8	39	3.4×10^{-5}	8.9×10^{-7}	1.3
0235+164	200	750	3.0	15	25	4.3×10^9	1.9	1.5	10	130	1.9×10^{-3}	1.5×10^{-5}	4.3
S5 0716+714	900	3.0×10^4	2.9	20	15	2.7×10^9	2.0	0.089	0.14	1.4×10^4	0.85	6.2×10^{-5}	15
OJ 287	350	4.0×10^4	4.1	20	15	1.0×10^9	1.6	0.53	8.3	66	0.042	6.3×10^{-4}	2.6
W Comae	800	2.1×10^4	2.6	30	15	1.9×10^9	2.0	0.014	0.021	560	0.037	6.6×10^{-5}	0.68
3C 66A	750	1.3×10^4	2.8	10	30	1.2×10^9	2.0	0.32	1.2	24	6.5×10^{-4}	2.7×10^{-5}	0.57

Notes.
[a] Magnetic field in units of Gauss.
[b] Kinetic luminosity in relativistic electrons in units of 10^{44} erg s^{-1}.
[c] Kinetic luminosity in relativistic protons in units of 10^{48} erg s^{-1}.
[d] Partition fractions defined as $\epsilon_{ij} \equiv L_i/L_j$.
[e] Minimum allowed variability timescale in hours.

objects and FSRQs, and neither are the characteristic electron energies (represented by $\gamma_{e,1}$) systematically different between the two classes of objects. If charge neutrality in blazar jets is provided by cold protons (rather than positrons), our fits indicate that the kinetic energy carried by the jets should be dominated by protons.

4.2. Hadronic Model Fits

Overall, we find that the SEDs of BL Lac objects, both IBLs (Figure 9) and LBLs (Figure 8), can be well represented with our model. The typically low ratio of γ-ray to X-ray flux and the hard γ-ray spectra observed in BL Lac objects (as compared to FSRQs) is naturally obtained by photo-pion-induced cascade emission with substantial contributions from proton-synchrotron radiation. In some cases, an additional contribution from the leptonic SSC emission aids in producing the observed X-ray flux. However, even though the addition of photo-pion-induced cascade emission to a proton-synchrotron component is, in principle, able to reproduce concave γ-ray spectra, the steep upturn of the *Fermi*-LAT spectrum of 3C 66A and W Comae at GeV energies is also still not well represented by this model, and may indicate the need for an additional emission component (possibly from muon/pion synchrotron radiation, with consequences for the values of the fit parameters). We note that the required power in relativistic protons, L_p, is very large, in the range $\sim 10^{47}$–10^{49} erg s^{-1}, which is significantly higher than the observed radiative luminosities of these objects.

Fits within the framework of the hadronic model to the SEDs of the FSRQs in our sample are shown in Figure 7. Although the hadronic model appears to satisfactorily fit most of the snapshot SEDs, the typically observed spectral break at GeV energies seems problematic in the cases of 3C 273 and 3C 279.

Also, here the γ-ray component is dominated by proton-synchrotron radiation, with some contribution from proton-initiated pair cascade emission above ~ 10 GeV. The too steep decline of the proton-synchrotron emission at a few GeV may indicate too steep a decline of the radiating proton distribution in the cutoff region (here considered a hard cutoff), and hence possibly an impact of the acceleration mechanism in this region

(e.g., Protheroe 2004; Aharonian 2000). The observed hard X-ray to soft γ-ray spectral shapes can be fitted if proton-synchrotron emission is the dominant radiation channel (in order not to overpredict the X-ray flux due to reprocessing of UHE γ-ray emission in cascades). This indicates the presence of high magnetic field strengths in the emission region.

The hadronic FSRQ fits also require extreme jet powers, in some cases exceeding 10^{49} erg s^{-1} in relativistic protons.

In summary, we find that the hadronic model presented here provides satisfactory fits to most of the bright blazar SEDs of our sample. However, the declining (in νF_ν) broken power-law shape observed in many *Fermi*-LAT spectra of FSRQs causes problems for adequate fits in two cases within the limits of this model. Fits to most objects have been achieved with magnetic fields in the range $B \sim 10$–30 G. All fits required proton acceleration to energies of $E_p \gtrsim 10^{17-18}$ eV. Nearly all model fits used a strong cascade component to aid modeling the high-energy GeV data. This leads to the requirement of a disproportionately large proton luminosity as compared to the magnetic field luminosity. As a consequence, in all hadronic model fit parameter sets presented here, the total jet power is dominated by protons. Alternatively, hadronic models that take charged π/μ synchrotron radiation into account (e.g., Mücke et al. 2003) could lower the strength of the pair cascade component, thereby reducing the proton contribution to the jet power at the expense of magnetic field power. In order to produce the observed (electron-synchrotron) IR–UV emission, the model requires lower characteristic electron energies for FSRQs ($\gamma_{e,1} \sim 100$) than for BL Lac objects ($\gamma_{e,1} \lesssim 10^3$), along with harder electron spectra in BL Lac objects. All our fits were achieved with characteristic Doppler factors of $D \sim 10$–30.

5. SUMMARY AND CONCLUSIONS

In this paper, we have described the development of new implementations of stationary, single-zone leptonic and hadronic models. Our leptonic model allows for arbitrary external photon sources, and solves self-consistently for an equilibrium between relativistic particle acceleration (injection), radiative cooling, and escape. Our hadronic model is based on the Kelner & Aharonian (2008) templates for the final products of
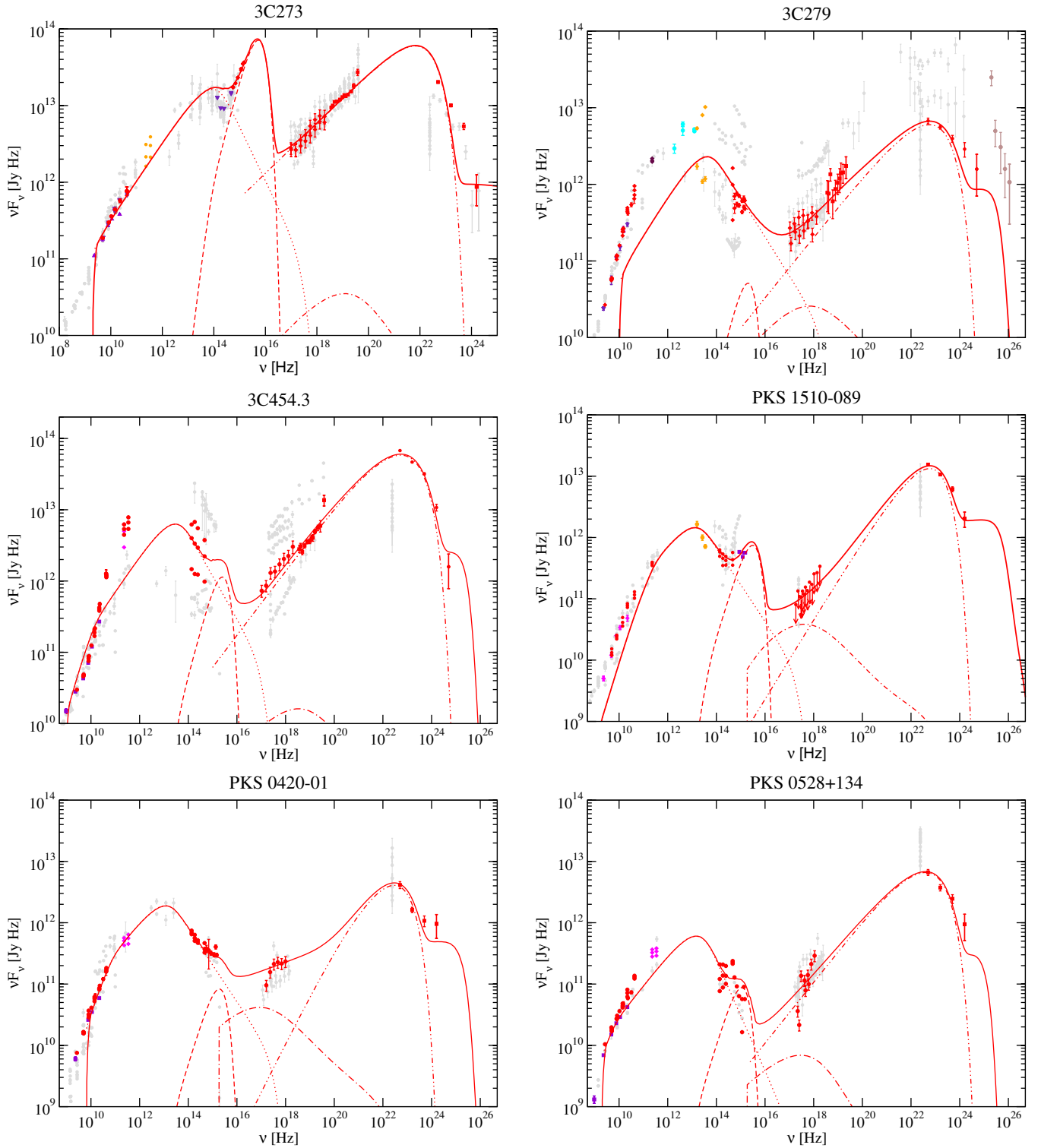
Figure 7. Hadronic model fits to the six FSRQs in our sample. See Table 3 for parameters. Dotted: electron-synchrotron; dashed: accretion disk; dot-dashed: SSC; dot-dot-dashed: proton-synchrotron.

(A color version of this figure is available in the online journal.)

photo-pion production, and uses a new, semianalytical method for calculating the output from UHE gamma-ray-induced pair cascades.

We have used both leptonic and hadronic models to fit the contemporaneous SEDs of 12 *Fermi*-LAT-detected blazars with good multiwavelength coverage and additional observational constraints on model parameters. We find that the SEDs of all

types of blazars can be well represented with leptonic models with parameters close to equipartition between the magnetic field and relativistic electrons in the emission region. However, our leptonic model is unable to provide a good fit to the hard *Fermi*-LAT spectrum of AO 0135+164. The problem lies in the mismatch between the very steep synchrotron (IR–optical–UV) continuum, as opposed to the very hard γ-ray spectrum, and
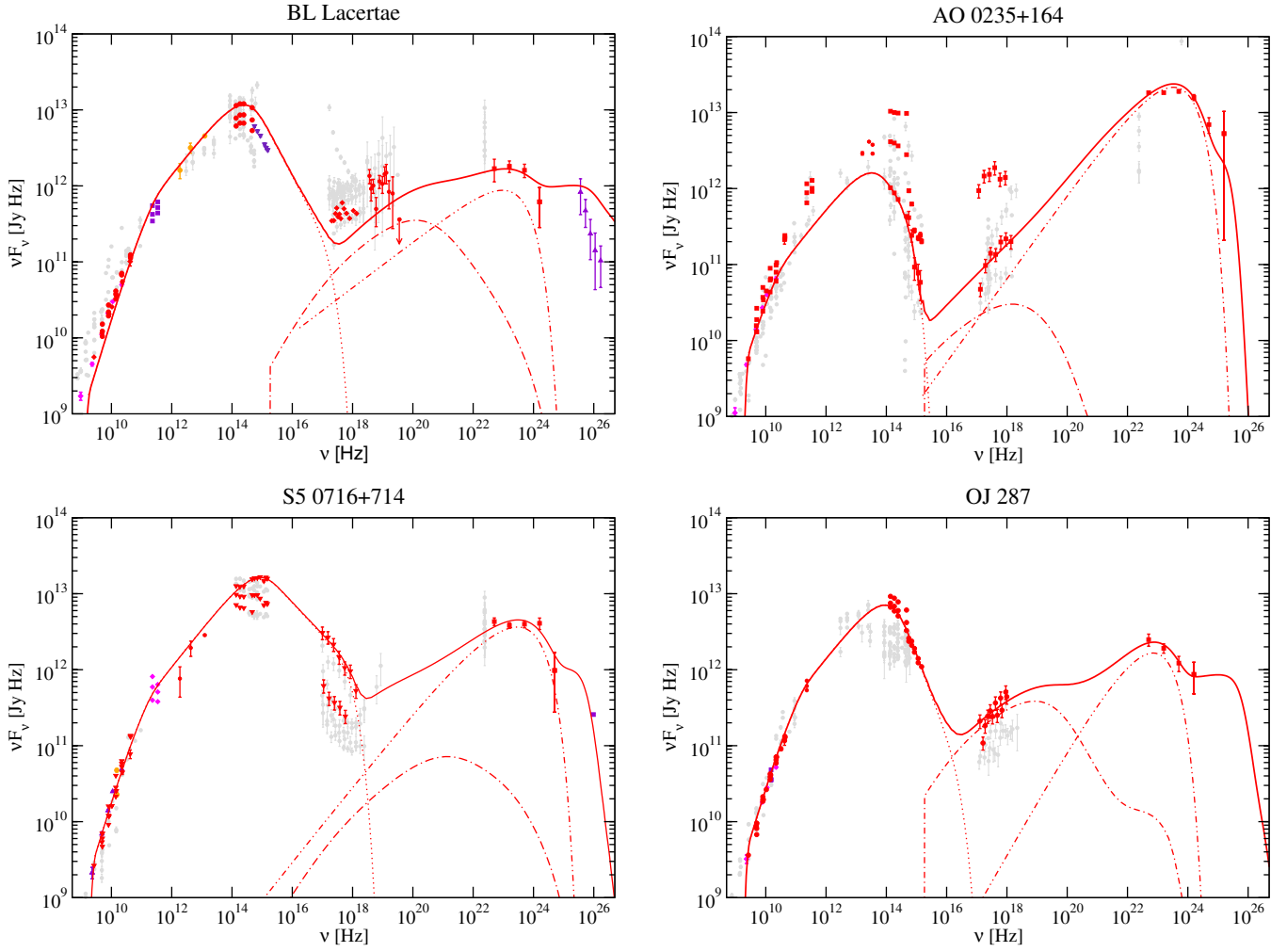
Figure 8. Hadronic model fits to the four LBLs in our sample. See Table 3 for parameters.
(A color version of this figure is available in the online journal.)
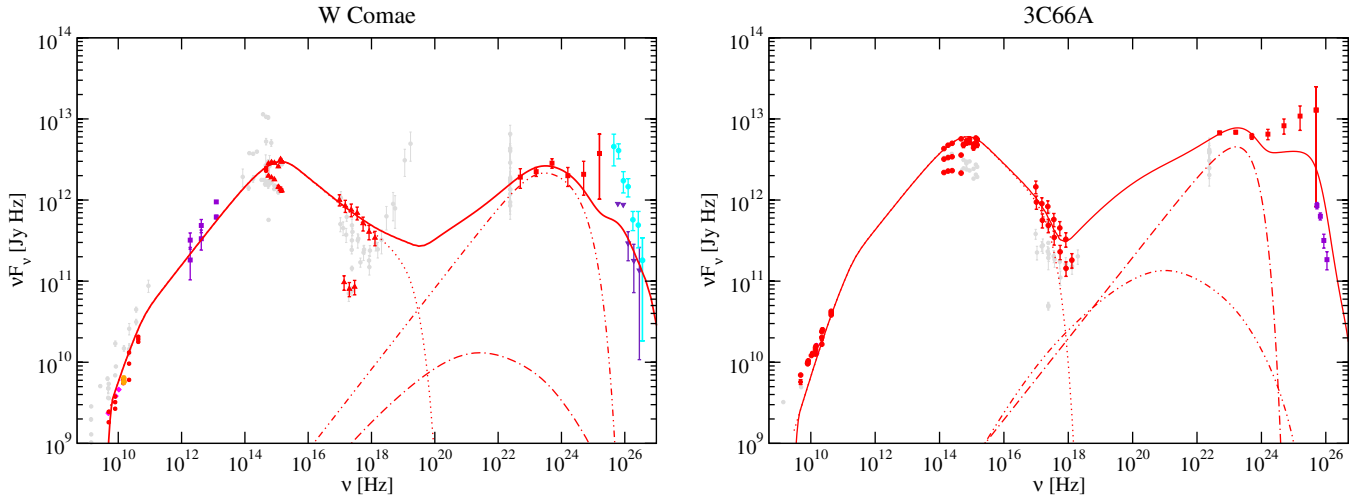
Figure 9. Hadronic model fits to the two IBLs in our sample. See Table 3 for parameters.
(A color version of this figure is available in the online journal.)

Klein–Nishina effects at the highest γ-ray energies. We confirm that even intermediate BL Lac objects are more appropriately fit including an external radiation field as a source for Compton scattering to produce the observed γ-ray emission. FSRQs are characterized by systematically more powerful jets, but lower bulk Lorentz factors and softer electron spectra than BL Lac objects. If charge neutrality in blazar jets is provided by cold protons (rather than relativistic positrons), our fits indicate that those protons are dominating the kinetic power carried by the jets by about an order of magnitude.

13

The hadronic model presented here has difficulty describing the GeV break in the SEDs of two FSRQs, but provides appropriate fits for all other blazars in our sample. However, the fits require very large powers in relativistic protons, of $L_P \sim 10^{47}$–10^{49} erg s^{-1}, in most cases dominating the total power in the jet.

REFERENCES

Abdo, A. A., Ackermann, M., Agudo, I., et al. 2010, ApJ, 716, 30
Abdo, A. A., Ackermann, M., Ajello, M., et al. 2011, ApJ, 726, 43
Acciari, V. A., Aliu, E., Arlen, T., et al. 2009a, ApJL, 690, L126
Acciari, V. A., Aliu, E., Arlen, T., et al. 2010a, ApJL, 708, L100
Acciari, V. A., Aliu, E., Arlen, T., et al. 2010b, ApJL, 715, L49
Acciari, V. A., Aliu, E., Aune, T., et al. 2009b, ApJ, 707, 612
Acciari, V. A., Aliu, E., Beilicke, M., et al. 2008, ApJL, 684, L73
Aharonian, F. A. 2000, NewA, 5, 377
Aharonian, F. A., Akhperjanian, A. G., Bazer-Bachi, A. R., et al. 2007, ApJL, 664, L71
Albert, J., Aliu, E., Anderhub, H., et al. 2007, ApJ, 669, 862
Albert, J., Aliu, E., Anderhub, H., et al. 2008, Sci, 320, 1752
Atoyan, A., & Dermer, C. D. 2003, ApJ, 586, 79
Begelman, M. C., Fabian, A. C., & Rees, M. J. 2008, MNRAS, 384, L19
Blandford, R. D., & Znajek, R. L. 1977, MNRAS, 179, 433
Blażejowski, M., Sikora, M., Moderski, R., & Madejski, G. M. 2000, ApJ, 545, 107
Bloom, S. D., & Marscher, A. P. 1996, ApJ, 461, 657
Böttcher, M. 2010, in Proc. Fermi Meets Jansky, MPIfR, Bonn, ed. T. Savolainen, E. Ros, R. W. Porcas, & J. A. Zensus (Bonn: MPIfR), 41
Böttcher, M. 2012, in Relativistic Jets of Active Galactic Nuclei, ed. M. Böttcher, D. Harris, & H. Krawczynski (Berlin: Wiley-VCH), chap. 2
Böttcher, M., Basu, S., Joshi, M., et al. 2007, ApJ, 670, 968
Böttcher, M., & Bloom, S. D. 2000, AJ, 119, 469
Böttcher, M., & Chiang, J. 2002, ApJ, 581, 127
Böttcher, M., & Dermer, C. D. 2010, ApJ, 711, 445
Böttcher, M., Mause, H., & Schlickeiser, R. 1997, A&A, 324, 395
Böttcher, M., Reimer, A., & Marscher, A. P. 2009, ApJ, 703, 1168
Celotti, A., & Ghisellini, G. 2008, MNRAS, 385, 283
Courvoisier, T., Robson, E. I., Hughes, D. H., et al. 1988, Natur, 335, 330
D'Arcangelo, F. D., Marscher, A. P., Jorstad, S. G., et al. 2007, ApJL, 659, L107
Dermer, C. D., & Menon, G. 2009, High Energy Radiation from Black Holes (Princeton, NJ: Princeton Univ. Press)
Dermer, C. D., & Schlickeiser, R. 1993, ApJ, 416, 458
Fan, J. H., Zhang, Y. W., Qian, B. C., et al. 2009, ApJS, 181, 466
Finke, J. D., & Dermer, C. D. 2010, ApJL, 714, L303
Finke, J. D., Razzaque, S., & Dermer, C. D. 2010, ApJ, 712, 238

Furniss, A., Fumagalli, M., Danforth, C., Williams, D. A., & Prochaska, J. X. 2013, ApJ, 766, 35
Georganopoulos, M., & Kazanas, D. 2003, ApJL, 594, L27
Ghisellini, G., Celotti, A., Fossati, G., Maraschi, L., & Comastri, A. 1998, MNRAS, 301, 451
Ghisellini, G., Tavecchio, F., Foschini, L., et al. 2010, MNRAS, 402, 497
Graff, P. B., Georganopoulos, M., Perlman, E. S., & Kazanas, D. 2008, ApJ, 689, 68
Hartman, R. C., Böttcher, M., Aldering, G., et al. 2001, ApJ, 553, 683
Hovatta, T., Valtaoja, E., Tornikoski, M., & Lähteenmäki, A. 2009, A&A, 498, 723
Jorstad, S. G., Marscher, A. P., Lister, M. L., et al. 2005, AJ, 130, 1418
Jorstad, S. G., Marscher, A. P., Mattox, J. R., et al. 2001, ApJS, 134, 181
Joshi, M., & Böttcher, M. 2010, ApJ, 727, 21
Kelner, S. R., & Aharonian, F. A. 2008, PhRvD, 78, 034013
Kusunose, M., Takahara, F., & Li, H. 2000, ApJ, 536, 299
Li, H., & Kusunose, M. 2000, ApJ, 536, 729
Lister, M., Cohen, M. H., Homan, D. C., et al. 2009, AJ, 138, 1874
Lyubarsky, Y. E. 2011, MNRAS, 402, 353
Madejski, G. M., Sikora, M., Jaffe, T., et al. 1999, ApJ, 521, 145
Mankuzhiyil, N., Ansoldi, S., Persic, M., & Tavecchio, F. 2011, ApJ, 733, 14
Mannheim, K., & Biermann, P. L. 1992, A&A, 253, L21
Marscher, A. P., & Gear, W. K. 1985, ApJ, 298, 114
Marscher, A. P., Jorstad, S. G., Larionov, V. M., et al. 2010, ApJL, 710, L126
Maraschi, L., Celotti, A., & Ghisellini, G. 1992, ApJL, 397, L5
Massaro, E., Mantovani, F., Fanti, R., et al. 2001, A&A, 374, 435
Mastichiadis, A., & Kirk, J. G. 1997, A&A, 320, 19
Mücke, A., Engel, R., Rachen, J. P., Protheroe, R. J., & Stanev, T. 2000a, CoPhC, 124, 290
Mücke, A., & Protheroe, R. J. 2000, in AIP Conf. Proc. 515, GeV–TeV Gamma-ray Astrophysics Workshop: Towards a Major Atmospheric Cherenkov Detector VI, ed. B. L. Dingus, M. H. Salamon, & D. B. Kieda (Melville, NY: AIP), 149
Mücke, A., & Protheroe, R. J. 2001, APh, 15, 121
Mücke, A., Protheroe, R. J., Engel, R., Rachen, J. P., & Stanev, T. 2003, APh, 18, 593
Mücke, A., Rachen, J. P., Engel, R., et al. 2000b, NuPhS, 880, 8
Mukherjee, R., Böttcher, M., Hartman, R. C., et al. 1999, ApJ, 527, 132
Palma, N., Böttcher, M., de la Calle, I., et al. 2011, ApJ, 735, 60
Peterson, B. M., Ferrarese, L., Gilbert, K. M., et al. 2004, ApJ, 613, 682
Pian, E., Falomo, R., & Treves, A. 2005, MNRAS, 361, 919
Prandini, E., Bonnoli, G., Maraschi, L., Mariotti, M., & Tavecchio, F. 2010, MNRAS, 405, L76
Protheroe, R. J. 2004, APh, 21, 415
Pucella, G., Vittorini, V., D'Ammando, F., et al. 2008, A&A, 491, L21
Raiteri, C. M., Villata, M., Capetti, A., et al. 2009, A&A, 507, 769
Raiteri, C. M., Villata, M., Chen, W. P., et al. 2008a, A&A, 485, L17
Raiteri, C. M., Villata, M., Larionov, V. M., et al. 2008b, A&A, 480, 339
Raiteri, C. M., Villata, M., Larionov, V. M., et al. 2008c, A&A, 491, 755
Sambruna, R. M., Urry, C. M., Maraschi, L., et al. 1997, ApJ, 474, 639
Sasada, M., Uemura, M., Arai, A., et al. 2008, PASJ, 60, L37
Schlickeiser, R. 1996, A&AS, 120, 481
Sikora, M. 2011, in IAU Symp. 275, Jets at all Scales, ed. G. Romero, R. Sunyaev, & T. Bellon (Cambridge: Cambridge Univ. Press), 59
Sikora, M., Begelman, M., & Rees, M. 1994, ApJ, 421, 153
Sokolov, A., Marscher, A. P., & McHardy, I. A. 2004, ApJ, 613, 725
Spada, M., Ghisellini, G., Lazzati, D., & Celotti, A. 2001, MNRAS, 325, 1559
Tagliaferri, G., Ghisellini, G., Giommi, P., et al. 2000, A&A, 354, 431
Takalo, L. O., Sillanpaeae, A., Pursimo, T., et al. 1996, A&AS, 120, 313
Tavecchio, F., & Ghisellini, G. 2008, MNRAS, 385, L98
Vasudevan, R. V., & Fabian, A. C. 2009, MNRAS, 392, 1124
Villata, M., Raiteri, C. M., Kurtanidze, O. M., et al. 2002, A&A, 390, 407
Xie, Z. H., Hao, J. M., Du, L. M., Zhang, X., & Jia, Z. L. 2008, PASP, 120, 477